

Case History

Forward modeling and 3D inversion of electromagnetic data collected over the McArthur River uranium deposit in the Athabasca Basin, Canada

Reza Mir¹, Peter Fullagar², Mehrdad Darijani³, Richard Smith¹, Shawn Scott⁴, Martin Ross⁴, Pejman Shamsipour⁵, Michel Chouteau⁵, Kevin Ansdell⁶, and Mohamed Gouiza⁷

ABSTRACT

Detection and assessment of the deeply buried high-grade uranium deposits in the Athabasca Basin rely on geophysical methods to map conductive rocks. Variable Quaternary surface cover can mask the anomalous signals from depth and affect the interpretation of inverted conductivity models. We present the analysis of several electromagnetic (EM) modeling studies and two field data sets to demonstrate the effects of varying Quaternary cover resistivity and thickness, on the ability to resolve the parameters of underlying sandstone, alteration, and basement conductors. Synthetic data, assuming a typical shallow EM sounding system and realistic resistivities found in the Athabasca Basin, indicate that resistivity and thickness parameters of the Quaternary cover can be separately recovered in cases in which this cover is more conductive than the underlying sandstone, but not when the

cover is significantly more resistive. A 3D modeling study indicates that by using airborne EM data, it is possible to detect a basement conductor of 20 S at a depth of at least 600 m below the surface, even in the presence of Quaternary cover thickness variations of the up to 20% (40–60 m). Furthermore, although Quaternary cover variations and deeper sandstone alteration can produce comparable anomalous signal amplitudes in a time-domain EM response, their effects are most visible in distinctly separate time windows. Ground-penetrating radar and other data to characterize the Quaternary cover in the McArthur River area indicate that this cover consists mostly of sandy tills ranging in thickness from 0 to 117 m. Constrained 3D inversion of an airborne EM data set from the same area indicates basement conductors consistent with the depth and location of a known fault. Elevated conductivity in the sandstone by up to a factor of two over the background values could indicate possible alteration.

INTRODUCTION

Unconformity-related uranium (URU) deposits in the Athabasca Basin of Canada are a major source of the global supply of uranium (IAEA, 2018). These high-grade ore bodies occur close to the

unconformity between the basin and the underlying basement rock and present a challenging class of economic targets for mineral exploration because they can be deeply buried and volumetrically small (Jefferson et al., 2007). Consequently, their detection and subsequent assessment has relied heavily on geophysical methods

Manuscript received by the Editor 7 April 2021; revised manuscript received 8 October 2021; published ahead of production 16 December 2021; published online 15 February 2022.

¹Laurentian University, Harquail School of Earth Sciences, Sudbury, Ontario P3E 2C6, Canada. E-mail: reza.mir@gmail.com (corresponding author); rsmith@laurentian.ca.

²Fullagar Geophysics Pty Ltd, Blackmans Bay 7052, Australia. E-mail: peter@fullagargeophysics.com.

³Memorial University of Newfoundland, Department of Earth Sciences, St. John's, Newfoundland A1B 3X7, Canada. E-mail: m.darijani@mun.ca.

⁴University of Waterloo, Department of Earth and Environmental Sciences, Waterloo, Ontario N2L 3G1, Canada. E-mail: shawn.scott@uwaterloo.ca; maross@uwaterloo.ca.

⁵Polytechnique Montréal, Department of Civil, Geological and Mining Engineering, Montreal, Quebec H3C 3A7, Canada. E-mail: pejman.shamsipour@gmail.com; michel.chouteau@polymtl.ca.

⁶University of Saskatchewan, Department of Geological Sciences, Saskatoon, Saskatchewan S7N 5E2, Canada. E-mail: kevin.ansdell@usask.ca.

⁷University of Saskatchewan, Department of Geological Sciences, Saskatoon, Saskatchewan S7N 5E2, Canada and University of Leeds, School of Earth and Environment, Leeds LS2 9JT, UK. E-mail: m.gouiza@leeds.ac.uk.

© 2022 Society of Exploration Geophysicists. All rights reserved.

(McMullan et al., 1987; Matthews et al., 1997; Powell et al., 2007). Conventionally, exploration in the area has been focused on conductive anomalies in the basement due to the presence of graphitic pelites associated with uranium mineralization as well as mapping prospective structures (Jefferson et al., 2007; Powell et al., 2007). Structurally controlled fluid flow along the unconformity at the intersection with major faults is thought to be responsible for the formation of the deposits. As a result, the quantity of collected geophysical data is greatest in the proximity of these faults. Another potential focus of exploration is alteration associated with mineralizing fluid flow within the overlying sedimentary rocks, but this has proven much more challenging from a geophysical perspective. This is mainly because the subtle signals from the weak conductivity contrasts associated with alteration in the sandstones are masked by the presence of Quaternary deposits of variable thickness at the surface and strong graphitic conductors in the basement. The alteration zones associated with basement-hosted deposits in the Athabasca Basin consist mostly of chlorite, muscovite, and coarse-grained illite (Alexandre et al., 2005; Cloutier et al., 2009). Smith et al. (2010) argue that the early time data from the TEMPEST airborne electromagnetic (AEM) system are able to detect sandstone alteration at the Millennium deposit above the graphitic horizon in the basement. Ground resistivity methods can sometimes identify more conductive zones associated with sandstone alteration (McMullan et al., 1987; Matthews et al., 1997; Powell et al., 2007; Long et al., 2017), but resistivity data can be difficult and expensive to acquire in the Athabasca Basin. If the alteration reduces the density of the sandstone, then gravity methods might be successful in detecting the associated signature (McMullan et al., 1987; Matthews et al., 1997); however, variations in the thickness and density of near-surface Quaternary deposits can mask these subtle anomalies. To better interpret geophysical data, the physical properties and

thickness of the Quaternary cover must be known. Such information is necessary to forward model data or constrain geophysical inversions to obtain accurate models at depths close to the unconformity or in the alteration zones in the overlying sandstone. Because electrical resistivity is one of the main physical parameters for exploration in the Athabasca Basin, knowledge of resistivity and depth extent associated with Quaternary surface cover is greatly desired. This is particularly true if the cover thickness as estimated from resistivity contrasts agrees with estimated thickness based on anomalous density contrasts. Rapid and relatively inexpensive electromagnetic (EM) surveys that probe the shallow subsurface are ideal tools if they can estimate parameters of the Quaternary sediments or identify alteration in the sandstone.

In this paper, we present the geologic background for the area of study in the Athabasca Basin and the McArthur River uranium deposit. This is then followed by several 1D and 3D modeling studies with realistic physical property parameters from the study area that show the ability of ground and airborne EM data to resolve parameters of Quaternary surface cover and those of conductive targets at depth. We then show the analysis and interpretation of two EM field data sets from the survey area: (1) a ground-penetrating radar (GPR) survey to determine the Quaternary cover characteristics and (2) an AEM data set to determine conductive targets at depth. Finally, we draw a few general conclusions based on the modeling of synthetic data and analysis of the field EM data.

GEOLOGIC BACKGROUND

The Athabasca Basin is situated in northern Saskatchewan and Alberta. It hosts URU deposits that are located along reactivated basement faults where they cut the unconformity between the late Paleoproterozoic to Mesoproterozoic sandstones in the basin and the underlying metamorphosed and complexly deformed Archean and Paleoproterozoic basement rocks of the Rae and Hearne Provinces and the Taltson Magmatic Zone (Figure 1; Jefferson et al., 2007).

Most of the deposits in the eastern Athabasca Basin are associated with structures that lie within the transition zone between the tightly folded Paleoproterozoic metasedimentary rocks cored by Archean granitoid gneiss in the Wollaston Domain and the Archean-dominated Mudjatik Domain. The geologic and structural relationships of the basement rocks in the Wollaston-Mudjatik Transition Zone have been detailed by Annesley et al. (2005), Tran et al. (2008), and Jeanneret et al. (2016). The regional scale geometry of the basement rocks, including the development of ductile shear zones, resulted from accretionary and collision events during the formation of the Trans-Hudson Orogen between approximately 1.86 and 1.76 Ga (Ansdell, 2005; Corrigan et al., 2009). As a consequence, the basement rocks in the study area consist of complexly interfolded Archean granitic gneiss, and Paleoproterozoic pelites, graphitic pelites, and quartz-rich rocks (McGill et al., 1993; Card and Heath, 2015; Rogers et al., 2017). The rocks of the Hearne Province, immediately below the unconformity,

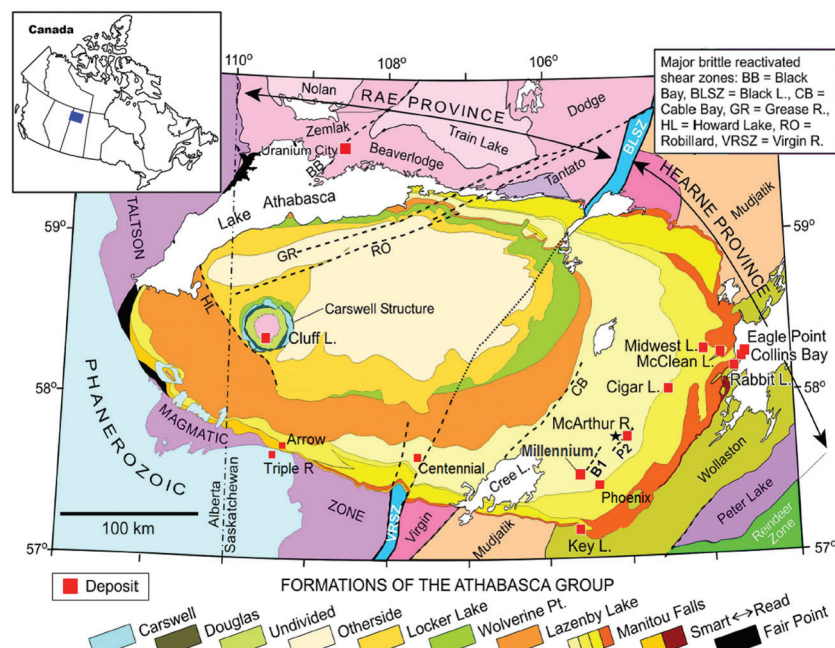


Figure 1. Geologic setting of the Athabasca Basin together with some of the main URU deposits in the region. The dashed lines indicate some of the major reactivated fault zones. The black star close to McArthur River marks the location of the VTEM survey presented in this paper (figure modified from Jefferson et al., 2007).

were weathered before the basin sandstones were deposited, as an interpreted residual paleo-regolith underlies the basal unconformity (Hoeve and Sibbald, 1978; MacDonald et al., 1985). Some of the basement shear zones were later reactivated under brittle conditions and acted as fluid conduits during mineralization and alteration events after the Athabasca Basin formed at approximately 1600 Ma or younger (Alexandre et al., 2009). An important example of such a shear zone is the northeast–southwest-oriented P2 fault (McGill et al., 1993; Adlakha et al., 2015), which hosts the McArthur River uranium deposit located at the unconformity at a depth of approximately 550 m, within basement graphitic pelites. McArthur River is the largest high-grade uranium deposit in the world, containing proven and probable reserves of 1.062 Mt at an average grade of 16.46% U_3O_8 (Bronkhorst et al., 2012).

Overlying the McArthur River deposit are the sedimentary rocks of the Athabasca Supergroup that fill the basin and form the sandstone and conglomerate of the Manitou Falls Formation (Figure 1). These are divided into four major sedimentary sequences that formed mainly in fluvial, lacustrine, and aeolian environments with minor marine sediments in the uppermost units. In general, the sequences fine upward and all are sandstone-rich in the eastern part of the basin (Ramaekers and Catuneanu, 2004; Hiatt and Kyser, 2007). These units have very high quartz contents and were deposited in an alluvial fan to braided stream environment, with detritus being derived from the erosion of the Trans-Hudson Orogen to the east (Hiatt and Kyser, 2007; Ramaekers et al., 2007). The thickness of the Manitou Falls Formation increases to approximately 700 m at the western side of the study area. The P2 reverse fault at McArthur River extends for approximately 15 km, offsetting the unconformity by up to 80 m, and has generated splays in the overlying sandstones. Brittle faults have fractured the lowermost part of the Manitou Falls Formation, which was intensely silicified along the P2 fault during early diagenesis. The most intense alteration occurs in close proximity to (within tens of meters of) the ore bodies, where illite, chlorite, dravite, and kaolinite, which are broadly synchronous with mineralization, occur in the matrix in the quartz-rich sandstones and typically make up approximately 5% of the rock volume (McGill et al., 1993; Ng et al., 2013). Mineralization and alteration, dominated by illite and chlorite, in the basement rocks is more tightly constrained to the graphitic rocks in the P2 fault zone, which separates pelitic rocks in the hanging wall from quartzitic rocks in the footwall (McGill et al., 1993).

The Athabasca Supergroup sandstones are overlain by Quaternary glacial deposits. The most abundant of these surficial deposits are tills, which locally have a complex internal stratigraphy (Scott et al., 2017) and contain debris from the underlying sandstones and from the basement rocks external to the basin (Campbell, 2007). In this paper, the surficial Quaternary glacial cover is also referred to as overburden. The topographic features shown in Figure 2 are dominated by streamlined subglacial landforms (drumlins), indicating ice flow from the northeast to southwest. In the study area, the drumlins are relatively long (up to 2 km) and tall (more than 50 m in height) for this type of landform (Hillier et al., 2013). Sandstone outcrops are rare in the study area and are mainly present in the swales between drumlins. Their elevation suggests a relatively flat bedrock surface. Based on this assumption and the topography of the heavily drumlinized ground surface, the elevation difference between the top of drumlins and the lowest elevation in the area in Figure 2 (approximately 145 m) provides a first-order

approximation for the maximum thickness of Quaternary sediments in the study area.

MODELING STUDIES

In this section, the results of several 1D and 3D EM modeling studies are presented to investigate their implications for the interpretation of field data presented later in this paper.

1D EM modeling

Knowledge of overburden resistivity and thickness is important for interpreting inversions and constraining electrical resistivity to obtain more accurate models at depth. As a result, it is of practical value to know if these overburden parameters can be determined with a typical shallow EM sounding instrument, given the common values of resistivity for the overburden and sandstone in the Athabasca Basin. Therefore, we generate synthetic data assuming the use of a Geonics PROTEM/TEM47 system. This is a typical instrument used routinely in the industry for shallow resistivity sounding and overburden mapping. The TEM47 transmitter is field portable and, by selecting from a range of possible survey parameters, allows for stratigraphic mapping with high near-surface resolution. The horizontal loop EM sensor measures the voltage associated with the decay of the vertical magnetic fields due to the induced currents in the subsurface at multiple time channels after the transmitter current has switched off.

The synthetic data for this instrument are generated using EM1DTM (Farquharson and Oldenburg, 2006), a modeling and inversion routine used to simulate time-domain electromagnetic data

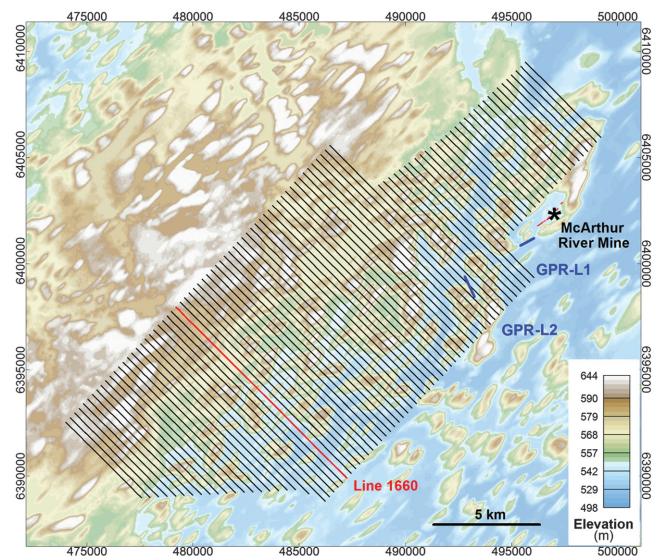


Figure 2. Map of the VTEM airborne survey lines (black) along with a color image of the topography in the area. The lines cover an area of approximately 250 km² with a spacing of 300 m. McArthur River mine (black asterisk) lies southeast of the northern part of the survey area. The edge of the nearest line is approximately 500 m away from the McArthur River mine. Topographic relief varies by approximately 70 m within the survey area. Line 1660, for which detailed results are presented in the paper, is marked in red. Blue lines mark the location of two GPR survey lines detailed in the paper. The location of the survey within the Athabasca Basin is marked in Figure 1.

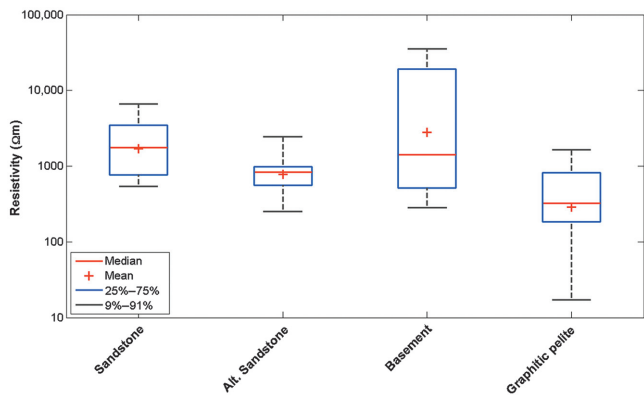


Figure 3. Resistivity of different lithologies in the Athabasca Basin and underlying basement in the McArthur River area, based on measurements on core and outcrop samples. There are 239 samples considered for this plot: sandstone (148), clay altered sandstone (illite, chlorite, dravite, and kaolinite assemblages; 17), basement rocks below unconformity (including pelite, pegmatite, quartzite, migmatite, psammite, and granite; 61), and graphitic pelite in the basement rocks below unconformity (13). Resistivity values were not available for the Quaternary cover in the study area. The values of overburden resistivity in the modeling studies of this paper range between 1000 and 16,000 Ωm . See Darjani (2019) and Vallée et al. (2019) for overview of physical property data sources.

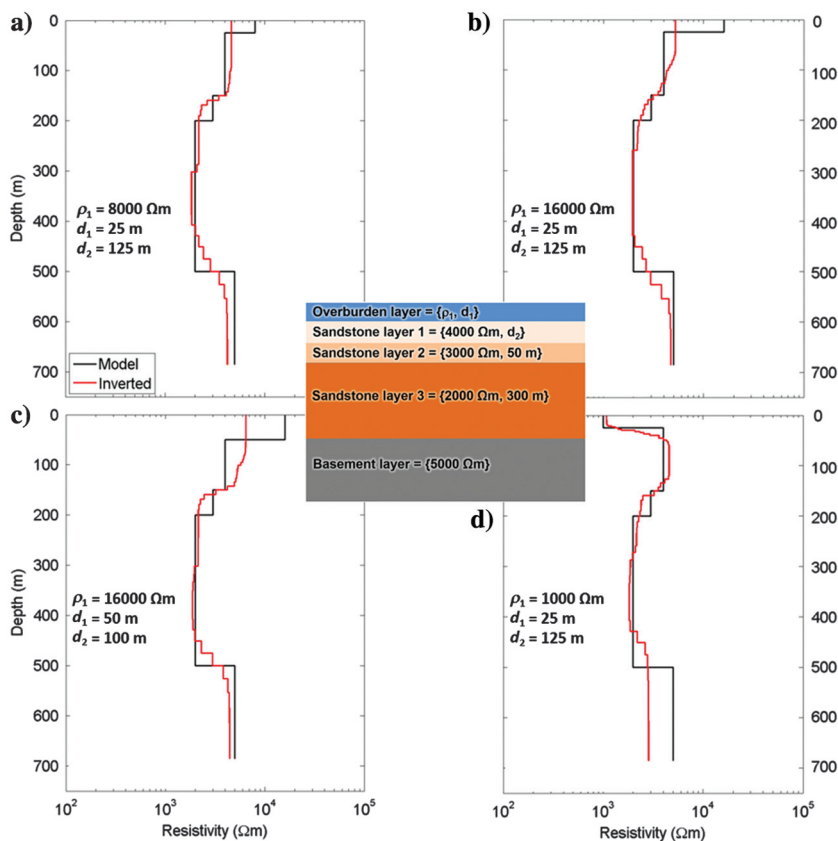


Figure 4. A series of 1D PROTEM modeling studies (A, B, C, and D) showing the ability of electromagnetic inversion methods to resolve overburden resistivity and thickness. A schematic of the model used is shown at center with overburden, sandstone, and basement layers. For each case (variations A–D), the response from this synthetic model (black) is forward calculated and corrupted with 5% random noise. These noisy data are then inverted with a 1D inversion algorithm (EM1DTM) to produce a model (red) that satisfies the data. See the “Discussion” section for an interpretation of these results.

measured as either magnetic field or its time derivative (voltage). The algorithm allows for an arbitrary transmitted current waveform driven through a horizontal loop. The receivers can be at any orientation with respect to the transmitter on the ground or in the air. For a given transmitter-receiver configuration and 1D earth model (conductivity varying only with depth), the forward-modeling routine computes the magnetic field response in the frequency domain using a matrix propagation, spectral expansion approach (Farquharson and Oldenburg, 1996; Farquharson et al., 2003), and converts the results into the time domain via the Fourier transform (Farquharson and Oldenburg, 1993). The inversion module of EM1DTM computes a model made up of a stack of layers with varying conductivities, able to reproduce the observed values of magnetic fields (or voltages) measured by a specified transmitter-receiver configuration. Computation of this layered-earth model is accomplished by iteratively solving a nonlinear inverse problem to minimize an objective function that is a combined measure of data misfit and model complexity. At each iteration, the problem is linearized about the current model and solved for updates to the model parameters. The iterations continue until a model is calculated that reproduces the measured data to within a specified misfit or threshold (Farquharson and Oldenburg, 2004).

The modeling studies of this paper make use of the available physical property data from the McArthur River region as shown in Figure 3. For the Quaternary cover, resistivity values were not available in the study area; therefore, the range of values used for modeling this unit are based on what is typically used for glacial sediments in the broader region (Darjani, 2019; Vallée et al., 2019) and vary between 1000 and 16,000 Ωm . Figure 4 shows four 1D models constructed with realistic resistivity values and the corresponding synthetic data, assuming a Geonics PROTEM/TEM47 sounding system optimized for overburden mapping (system settings are given in Table 1). For each model (in black), the EM decay response is first calculated, and then inverted with EM1DTM to produce a “best-guess” resulting model (in red), similar to what would be done with actual field data. The aim is to find out if it is possible to recover the resistivity-depth profile of the original model by inverting the calculated data. The inversion assumes no prior knowledge or constraints and takes as input the forward calculated data with an added 5% random noise and an initial resistive half-space model of 10,000 Ωm resistivity. The models examine two different situations depending on whether the Quaternary sediment cover is more resistive or conductive than the underlying sandstone. Models A, B, and C show the case of a resistive overburden overlying more conductive sandstone. In model A, an overburden of 25 m thickness with 8000 Ωm resistivity overlies a sandstone layer of 4000 Ωm and 125 m thickness. In this case, the inversion result replaces this structure with a single layer of thickness 150 m and resistivity of 4600 Ωm , which is approximately the

thickness-weighted average of the two original layers. In model B, the overburden resistivity is increased to 16,000 Ωm , the upper limit of resistivity likely to be encountered for surficial material, to give a factor of four contrast to the underlying sandstone, whereas all layer thicknesses remain the same. Again, the inversion result replaces the original structure of two different layers with a single layer, in this case, of thickness 150 m and resistivity of 5200 Ωm , which approximates the thickness-weighted average of the two original layers. Model C keeps the resistivity of overburden at 16,000 Ωm but increases the layer thickness by a factor of two to 50 m. Here, even with an increased thickness in overburden, it is not possible to resolve the resistivity and thickness parameters of the uppermost resistive layer separately. The final model in D depicts a conductive overburden of 1000 Ωm resistivity and 25 m thickness overlying sandstone layers with parameters similar to the other models. In this case, the inversion resolves the thickness and resistivity parameters of the conductive layer separately. Note that the conductive overburden layer in D results in the resistivity of the basement not being as well resolved as compared with that in models A, B, and C.

3D EM modeling

In this section, we present the results of a 3D modeling study to determine the possibility of detecting conductive targets (such as graphitic units) and other features (such as those associated with alteration in the sandstone) using AEM data, given typical values of resistivity for the lithologies and realistic values of the noise floor for an AEM system. We also consider the possible effect of overburden thickness variations in masking the signal from deep conductive targets of interest.

Here, we assume the use of an airborne EM instrument known as the versatile time-domain electromagnetic (VTEM) system. VTEM consists of a multiturn transmitter coil, and a set of smaller receiver coils mounted at its center, all towed below a helicopter. A periodic electrical current waveform is conducted through the transmitter coil, which induces a secondary current system in the earth below the instrument. The receiver coils record the time rate of change of the horizontal and vertical magnetic fields during the transmitter off-time at many different time channels. For the models presented here, VTEM receiver data were generated assuming a horizontal receiver loop of 1 m² area, measuring the time derivative of the induced vertical magnetic field (voltage) at the center of a coplanar transmitter loop of unit dipole moment. The receiver data are modeled for the same time channels as the VTEM system, given in Table 2, as measured with reference to the end of the transmitter waveform turn-off ramp. The transmitter current was modeled as a rectangular pulse of width 5.74 ms with an instantaneous switch-off. The real VTEM system has the same total pulse width, but a linear turn-off ramp of approximately 2 ms duration. Although the instantaneous switch-off presents an approximation, the error due to this is likely much smaller than errors as a result of these models being only an approximation of geologic reality. Moreover, these models are compared only with each other, and not to real field data. It is also important to note that this instantaneous switch-off is only used for these forward-

modeling studies. The inversion of the real VTEM data presented later in this paper uses the actual VTEM waveform.

The synthetic VTEM data for the models presented here are computed in the frequency domain using CSEM3DFWD (Ansari and Farquharson, 2013) for 150 frequencies over the range of 1–10 MHz. A Fourier transform (Newman et al., 1986; Jones et al., 2016) is used to calculate time-domain values at 44 time points corresponding to the VTEM time channels (Table 2). CSEM3DFWD is a routine based on the finite-element method that solves either for the electric field or the electric and magnetic potentials using nodal or edge-based elements that mesh the modeling area. To increase the accuracy of the computed-field values, the tetrahedral mesh that discretizes the modeling space is refined near the transmitter and receiver points or where the field gradient is highest, such as around places with rapid changes in conductivity.

Figure 5 presents the four models used in this study. The resistivity values for the different units are based on the average resistivities obtained from petrophysical sampling at McArthur River (Figure 3), and the depths and thicknesses of units are based on drilling at this site. These models comprise three distinct layers: overburden, sandstone, and basement. There are 10 EM readings at 30 m above ground with a station spacing of 100 m. The left-most receiver is defined to be at location 0 m on the profile. Model E is a three-layer structure (overburden, sandstone, and basement) used as reference to compare with the other models. Model F is identical to model E but with the addition of a strong dipping conductor (resistivity 1 Ωm , thickness 20 m, 45° dip, infinite strike extent) at a depth of 600 m directly below the center of the array of receivers. This thin, highly conductive, dipping conductor is a representation of a graphitic pelite unit associated with uranium mineralization. Model G adds a halo of alteration (resistivity 1000 Ωm , infinite strike extent) within the sandstone directly above the top of the conductor in the basement. Finally, model H represents a case in which the Quaternary cover thickness varies from 40 to 60 m above the conductor. This is meant to compare and contrast the effect of a varying surface cover thickness on the data with the case where alteration is present within the sandstone unit (model G). For these models, the features extend to either side of the EM survey line by 2 km, so that the models are effectively of infinite extent in

Table 1. Transmitter and receiver parameters for the modeling of data in Figure 4.

System setting	Value
Transmitter dipole moment	3 A in 40 × 40 m dipole, single turn loop
Transmitter base frequency	285 Hz
Transmitter turn-off time	2.5 μs
Receiver dipole moment	1 m radius loop, 10 turns
Receiver integration time	30 s
Receiver time gates (μs)	20 gates with centers at 6.81, 8.69, 11.13, 14.19, 18.07, 23.06, 29.44, 37.56, 47.94, 61.13, 77.94, 99.38, 126.7, 166.4, 206.0, 262.8, 335.2, 427.7, 545.6, and 695.9
Receiver noise	1 nV/m ²

These parameters are chosen based on typical instrument settings of a popular Geonics PROTEM/TEM47 system configured for shallow subsurface sounding and overburden mapping.

Table 2. Center of the time channels for the VTEM system as measured after the transmitter waveform turn-off ramp.

Channel number	Time (μ s)
1	21
2	26
3	31
4	36
5	42
6	48
7	55
8	63
9	73
10	83
11	96
12	110
13	126
14	145
15	167
16	192
17	220
18	253
19	290
20	333
21	383
22	440
23	505
24	580
25	667
26	766
27	880
28	1010
29	1161
30	1333
31	1531
32	1760
33	2021
34	2323
35	2667
36	3063
37	3521
38	4042
39	4641
40	5333
41	6125
42	7036
43	8083
44	9286

The same time channels are used for computing the response of the 3D models in Figure 5 and comparing their responses with each other in Figures 6–9.

the strike direction (perpendicular to the survey line). In all models, the topography is considered flat.

A comparison of the receiver responses for models E, F, G, and H is shown in Figure 6. Each plot shows the receiver response from these four models at one receiver position along the survey line. The red horizontal line indicates the minimum detectable signal level by the VTEM system. The response is mainly dominated by the basement conductor, and at this scale, it is difficult to discern the effects due to a varying overburden or sandstone alteration in the absolute signals. Therefore, the difference between these models is illustrated in more detail in Figures 7, 8, and 9, which present comparisons of received responses for models E and F, models F and G, and models F and H, respectively. The individual plots in each figure represent receiver positions along the profile; the positions shown are 0–800 m in increments of 100 m. The left axis (black curve) of each plot shows the absolute difference between the decay curves of the two models ($\text{model 1} - \text{model 2}$). This difference needs to be examined in reference to the minimum detectable signal size of the VTEM system, which is approximately $2 \times 10^{-4} \text{ pV/Am}^4$; when the signal falls below this threshold, it is no longer detectable by the system. Here, the dashed red vertical line indicates the last channel at which the signal difference is above this minimum detectable level. All channels left of the red vertical line register measurable changes in signal size. The right axis (blue curve) of each plot shows the difference in response between the models as a percentage, by normalizing the black curve to the average of the two model responses at each time channel using the equation, $100 \times \text{model 1} - \text{model 2} / 0.5 \times (\text{model 1} + \text{model 2})$. This percentage difference has the advantage of highlighting the channels that show the largest relative changes in response between the given models.

Figure 7 presents the comparison of models E and F. Here, the effect on the data due to a strong dipping conductor in the basement is investigated. The signal difference plots (black, left axis) show that for all receiver positions, the early channels (1–15) measure a detectable change in signal between the two models. This is seen as the signal change for these channels being above the minimum detectable threshold (dashed red line is well beyond channel 15) for all positions. However, because the absolute signal is very strong in these early channels, this change translates into a small relative difference of up to only approximately 5% at the maximum (blue, right axis). As one moves along the profile to stations near and above the conductor, beyond 300 m, the signal difference for the mid to late channels (>20) increases steadily and moves above the minimum detectable threshold so that more of the late channels register a measurable change (seen as the dashed red line moving steadily to the right). More importantly, the relative change is on the order of 200% for late channels up to the detection threshold. This is a far stronger effect than the relative change in the early channels, as expected for a deep conductor with a slow decay evident at late time.

Figure 8 shows the comparison between models F and G. This comparison looks for the effect on the data of a weak conductivity anomaly above the conductor at depth. This situation is potentially representative of a volume of alteration within the sandstone overlying the basement conductor. In this case, there is a detectable signal change due to the conductivity anomaly at all positions in the early to mid-channel range of 1–22. The largest relative change of up to 10% occurs in the mid-channel range of 10–22. The response in the later channels (>22) is dominated by the basement conductor at depth that is present in both models, and so the difference

between the responses from the two models in the late channels is below the threshold of detection by the system for all positions. Unlike Figure 7, the minimum threshold channel marked by the dashed red line does not move beyond channel 22.

The comparison between models F and H is shown in Figure 9. These plots investigate the effect of a varying overburden thickness on the signal from a deep conductor. Here, a 20% change in overburden thickness causes measurable changes in the first 20 channels. However, the largest variations, on the order of 5%–10%, occur at the earliest channels. The responses in the channels beyond 20 are dominated by the basement conductor, which is present in both models, and as a result, the difference between the responses for these channels is below the detection threshold for all positions.

FIELD DATA

Ground penetrating radar

A series of 14 GPR profiles totaling 9 km was acquired and processed near McArthur River to obtain information on the overburden thickness in areas of moderately resistive Quaternary cover (e.g., sandy till). A subset of that data, shown in Figure 2 as GPR-L1 and GPR-L2, is presented here to provide useful information on the nature of the Quaternary sediment cover and depth-to-bedrock in the study area. A 25 MHz MALA Rough Terrain Antenna system was used, consisting of a MALA ProEx control unit and a tug-along snake that hosts an unshielded transmitter and a receiver at 4 m spacing. This unit was towed behind an operator wearing the control unit in a backpack while a string chain was used, triggering the unit at 4 cm intervals with a time window of 1150 ns. Collected profiles were processed using ReflexW from Sandmeier Geophysical Research. Noise is reduced by stacking 25 traces (at 1 trace per 4 cm) and averaging them to get one trace per meter. Start time is shifted to remove dead time before the first direct-wave arrival and a subtract-mean (dewow) function is applied to remove drift in the data. An automatic gain function is then applied to equalize the amplitude down trace to correct for attenuation caused by material properties and geometric spreading losses (Cassidy, 2009). Finally, profiles are corrected for topography using the digital elevation model (DEM) of the area, and time/depth estimates are obtained via using hyperbolic curve fitting and local borehole data where possible.

For these data, depth of penetration and strength of reflectors varied significantly throughout the study area. Notably, the variation in signal

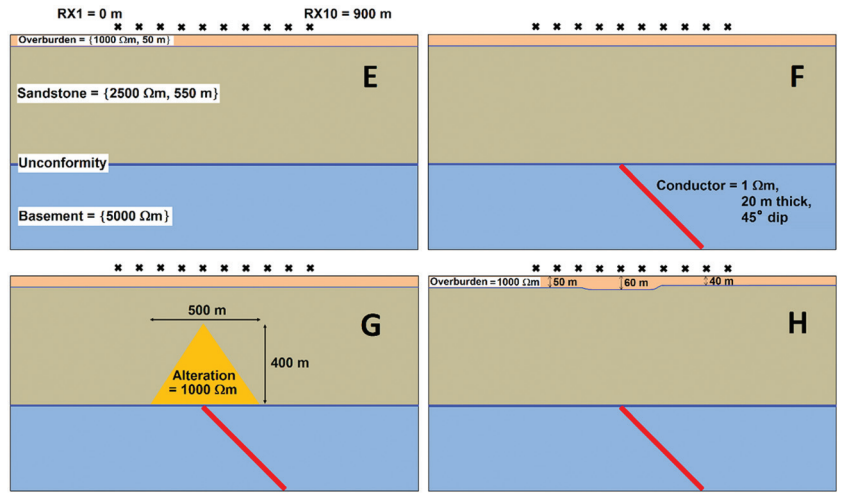


Figure 5. The four models considered for the VTEM study. The resistivity and thicknesses of the various units and features are shown on the model. There are 10 locations of coincident transmitter/receiver pairs at a height of 30 m above ground. Station spacing is 100 m, and the profile position of the first station at the far left is defined to be 0 m. (E) A simple model with overburden, sandstone, and basement. (F) A modified model with a conductor within the basement. The edge of the conductor is directly below the fifth receiver. (G) A model with a conductive alteration volume within the sandstone overlying a conductor within the basement. (H) A model with a conductor within the basement and varying overburden thickness. The overburden in this case varies in thickness from 50 m on the left to 60 m over the conductor to 40 m at the far right.

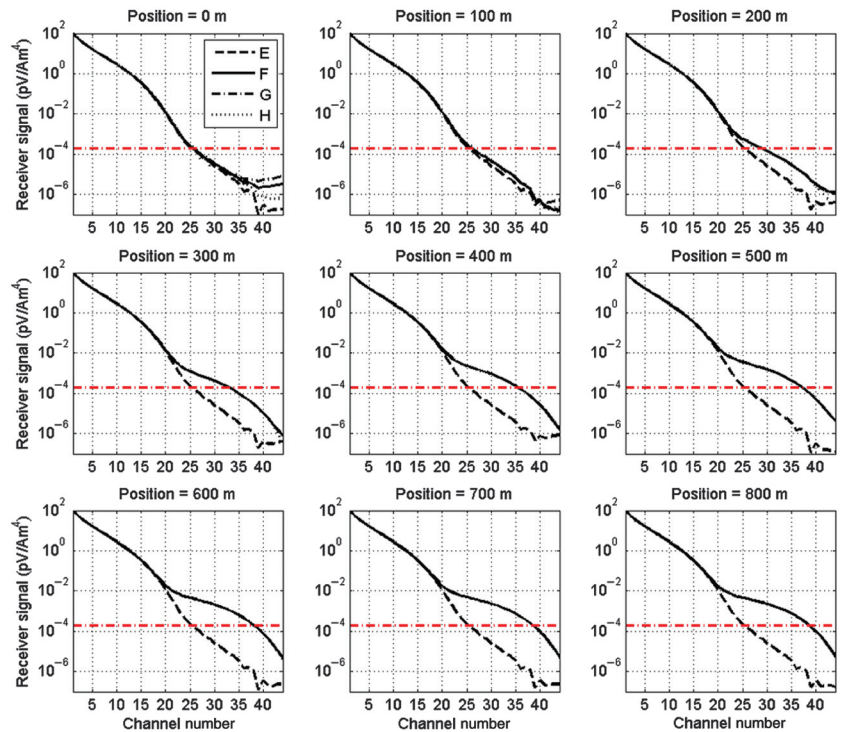


Figure 6. A comparison of the responses of the VTEM models E (reference), F (with basement conductor), G (with basement conductor plus alteration), and H (with basement conductor plus overburden variation) from Figure 5. Each plot shows the receiver response from these four models at one receiver position along the survey line. The transmitter and receiver have unit dipole moments. The red horizontal line indicates the minimum detectable signal level by the VTEM system. The difference between these models is illustrated in more detail in Figures 7–9.

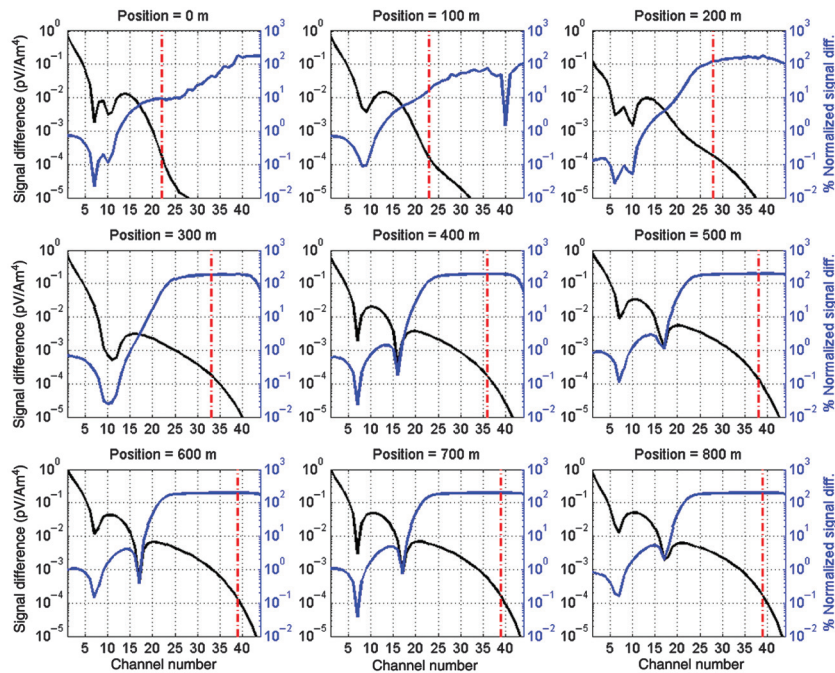


Figure 7. A comparison of VTEM models E and F from Figure 5. Each plot corresponds to one receiver position. The transmitter and receiver have unit dipole moments. The left axis (black curve) on each plot is the absolute difference in the decay curve between the two models. The right axis (blue curve) represents this difference as a percentage change in signal size by normalizing to the average signal (i.e., $100 \times |E - F| / 0.5 \times (E + F)$). The red vertical line indicates the last channel at which the signal difference is above the minimum detectable signal for the VTEM system.

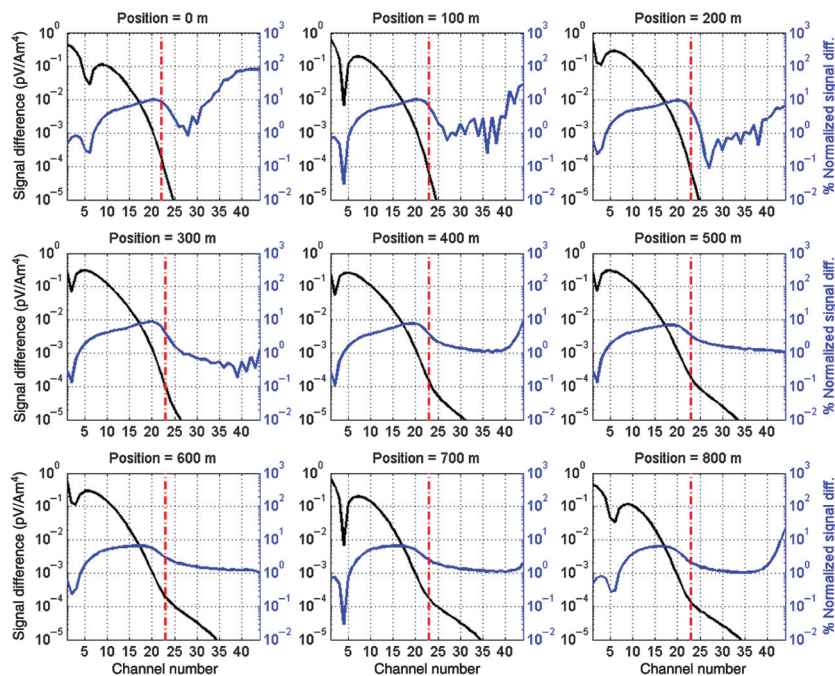


Figure 8. A comparison of VTEM models F and G from Figure 5. Each plot corresponds to one receiver position. The transmitter and receiver have unit dipole moments. The left axis (black curve) on each plot is the absolute difference in the decay curve between the two models. The right axis (blue curve) represents this difference as a percentage change in signal size by normalizing to the average signal (i.e., $100 \times |F - G| / 0.5 \times (F + G)$). The red vertical line indicates the last channel at which the signal difference is above the minimum detectable signal for the VTEM system.

penetration appears to be strongly dependent on surface materials, as well as depth to water table. Based on hyperbolic diffraction velocity estimations, the average ground wave velocity for the radar waves was estimated to be between 0.10 and 0.11 m/ns. Those estimations were consistent with constraints from diamond drillholes that intersected bedrock within 2–4 m of the GPR-interpreted depths at those velocities. The deepest resolvable radar signal penetration of approximately 55 m was achieved where coarser glacio-fluvial and aeolian sands occur at the surface. The depth of penetration was reduced on average by approximately 50% (down to 25 m) over till. In the study area, fine sands and silts are generally characterized by none to weak internal reflections, and coarse sand and gravel are characterized by multiple consistent flat or dipping contours with little signal attenuation. Till is a heterogeneous media and is evidenced by numerous arcuate reflections, whereas increased clay content causes attenuation of GPR signal.

Figure 10 shows a sample GPR profile approximately 680 m in length, the location of which is shown in Figure 2 as GPR-L1. Within the first 350 m of the profile, the top 5–10 m, which is devoid of reflections, is interpreted to be made of fine sand and sand and peat overlying till. Below this, a strong, wide, continuous reflector is assigned to the bedrock contact between overburden and sandstone. This interpretation is well supported by the stratigraphic description of available drill-holes along the line.

Another sample GPR profile is shown in Figure 11 (marked as GPR-L2 in Figure 2) to demonstrate the capability and limitations of GPR in resolving the overburden stratigraphy and the depth-to-bedrock. On this section, within intervals 0–300 and 450–600 m along profile, coarse sands and gravels occur close to surface, whereas for the interval 760–920 m, fine sands are the predominant material at the surface. Below these, a layer of till overlies the sandstone bedrock. The water table is interpreted as the strong, continuous reflector at a depth between 3 and 8 m. The control on the water table is given by a pond that was a few meters away from the profile at position $x \approx 700$ m. The free water surface in this pond was 2 m below the elevation of the profile. The bedrock interface between the overburden and the sandstone is delineated by a weak to moderate reflector observed at a depth between 30 and 40 m below surface. The reflector is lost because of till attenuation at 300–400 m and unclear beyond 750 m along the profile. The two boreholes in the vicinity of the GPR profile intersect the bedrock at a depth of approximately 40 and 29 m below $x = 0$ and 500 m, respectively, giving

confidence in our interpretation. However, GPR penetration depth in this area is limited to approximately 40 m. It is important to note that this only provides a minimum range thickness for the overburden because this profile was acquired on the edge of a drumlin as opposed to its top. The elevation difference between the top of the drumlin and the bedrock surface (obtained from the GPR and borehole data) indicates a maximum sediment thickness of approximately 117 m in this area.

AEM data

Figure 2 shows the location of the survey lines for a VTEM data set collected in 2013 over the Read Lake Project, near the McArthur River mine in the Athabasca Basin, Saskatchewan. The survey covers an area of approximately 250 km² with 889 line-km of magnetic and time-domain electromagnetic data at a line spacing of 300 m. The EM data were collected with the receiver at an average height of 31 m above ground and a sampling interval of 2.2 m along line. The transmitter and receiver were in a concentric-coplanar configuration. The transmitter loop had a diameter of 35 m with a peak dipole moment of 1,391,561 Am². The transmitter waveform consisted of an exponential increase in current followed by a sharp linear turn-off to zero of approximately 2 ms, forming a trapezoid waveform with a total pulse width of 5.74 ms and a base frequency of 30 Hz. The received data consist of the off-time decay of the vertical component of the induced magnetic field, sampled at 44 time channels ranging from 21 to 9286 μs (Table 2) measured with respect to the end of the turn-off ramp of the transmitter current. There was approximately 70 m of topographic relief within the survey region.

For the 3D inversion of this VTEM data set, we used VPem3D, which is an approximate 3D modeling and inversion routine for transient electromagnetic (TEM) data collected with a variety of common system configurations (Fullagar and Schaa, 2014). It can be used for airborne, ground, or borehole data. The code achieves faster run times than conventional 3D TEM inversion programs by transforming the data into the resistive limit (RL) (Stolz and Macnae, 1997; Macnae et al., 1999; Reid and Macnae, 2002). The RL at each observation point is the time integral of the magnetic field transient decay weighted by time,

$$RL = - \int t \frac{\partial B}{\partial t} dt. \quad (1)$$

The units of RL data presented in this paper are picoTesla millisecond (pTms). As an example, Figure 12 shows the multichannel VTEM data along line 1660, shown in Figure 2, together

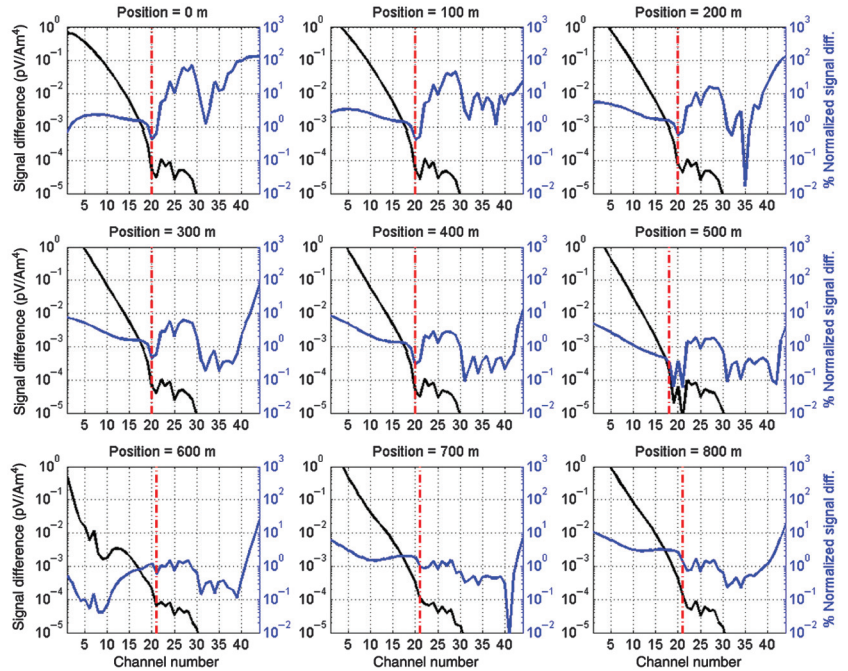


Figure 9. A comparison of VTEM models F and H from Figure 5. Each plot corresponds to one receiver position. The transmitter and receiver have unit dipole moments. The left axis (black curve) on each plot is the absolute difference in the decay curve between the two models. The right axis (blue curve) represents this difference as a percentage change in signal size by normalizing to the average signal (i.e., $100 \times |F - H| / (0.5 \times (F + H))$). The red vertical line indicates the last channel at which the signal difference is above the minimum detectable signal for the VTEM system.

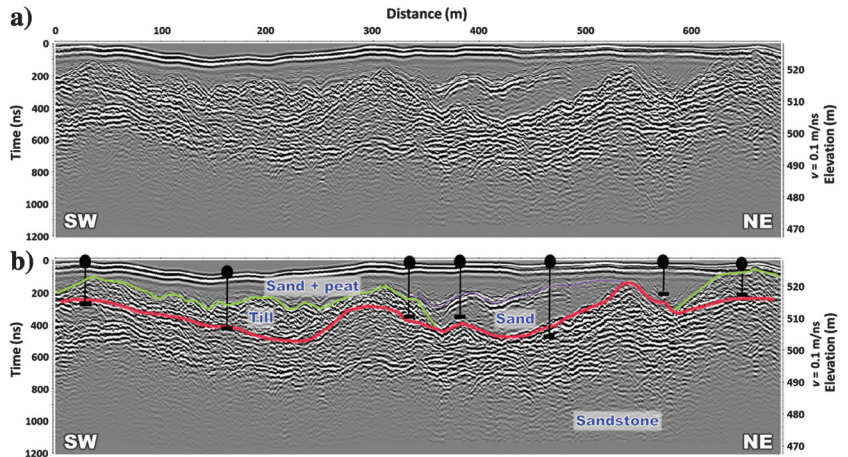


Figure 10. The GPR data collected and processed over a two-way traveltime window of 1200 ns, equivalent to a depth of approximately 60 m for an average velocity of 0.1 m/ns. This survey line is marked in Figure 2 as GPR-L1. (a) Uninterpreted section and (b) interpreted section showing a sequence of either sand or sand and peat over till or sandstone bedrock. Sand shows weak to no visible internal reflectors, whereas till creates many arcuate complex reflections due to textural heterogeneity (ranging from clay to boulders). The interpreted contact between the overburden and the sandstone is shown in red. Location of drillholes existing in the vicinity is shown by black circles, and depth-to-bedrock from the geologic logs is displayed by vertical black lines. Note the excellent correlation between the interpreted bedrock topography from GPR data and the depth-to-bedrock from existing drillholes.

with the RL data for the same line integrated over the entire 44 time channels from 21 to 9286 μs . This line was chosen because it traverses what appears to be one of the stronger conductors in this region. Calculating the RL allows the reduction of the multichannel TEM data into a single channel, which leads to a substantial gain in computational speed when doing an inversion. This gain in computational speed is achieved at the expense of losing the transient behavior that potentially contains information about the conductivity profile with depth. Some of this information can be recovered using starting conductivity models constructed from 1D inversions or conductivity-depth images. VPem3D facilitates integrated geologic interpretations by enabling inversion on geologic models, such that each model cell can be assigned a rock type as well as a physical property value (Fullagar and Pears, 2007). Constraints, such as drillhole pierce points in geologic contacts and ranges of physical properties for different units, can also be incorporated into the starting model.

It should be noted that as a result of inverting RL data (rather than the full multichannel TEM data), the conductivity units of the VPem3D inversion models being presented in this paper are not S/m, but rather a quantity that is proportional to conductivity in S/m. For simple conductive bodies, this quantity is dependent on size and shape of the body (Nabighian and Macnae, 1991). Therefore, the values of conductivity shown in our inverted models can be regarded as being proportional to S/m with an unknown constant of proportionality. In practice, this means that the numerical values at each location in a model should not be regarded as absolute conductivity, but rather seen in a relative sense when comparing conductive and resistive regions. For this reason, we designate the units of conductivity in the VPem3D inversion plots we present as having arbitrary units.

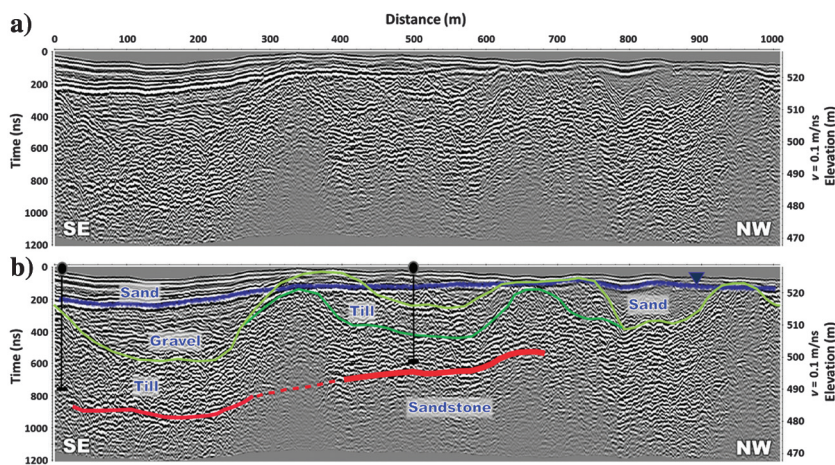


Figure 11. The GPR data collected and processed over a two-way traveltime window of 1200 ns, equivalent to a depth of approximately 60 m for an average velocity of 0.1 m/ns. This survey line is marked in Figure 2 as GPR-L2. (a) Uninterpreted section and (b) interpreted section showing a sequence of sand over gravel and till overlying the sandstone bedrock. Sand shows weak to no visible internal reflectors, gravel is evidenced by flat lying small reflections, and till creates many arcuate complex reflections due to textural heterogeneity (ranging from clay to boulders). The interpreted contact between the overburden and the sandstone is shown in red. Location of two drillholes existing in the vicinity is shown by black circles, and depth-to-bedrock from the geologic logs is displayed by vertical black lines. Note the good correlation between the interpreted bedrock topography from GPR data and the depth-to-bedrock from existing drillholes. The bedrock reflector is not clearly imaged beyond $x = 700$ m. Attenuation of the GPR signal in the ranges $x = 300$ – 400 and 900 – 1000 m can be attributed to higher clay content in the till. The water level is shallow (3–8 m) displayed by a dark blue line.

Figure 13 shows a map of the RL computed according to equation 1 for the entire survey area. The map also shows the location of interpreted conductors from historical ground EM surveys, projected to the surface (provided by Cameco, personal communication, 2017). The strength of a conductor refers to the conductivity-thickness product as interpreted from ground EM inversions and is indicated by the width of the black lines in the figure. It is apparent that although the RL is devoid of depth information, it does map the strongest conductors in the area. The slight apparent offset between the RL peak values and the indicated conductor axes is due to the dip of the buried conductors at depth. The conductors marked with black lines on the map that have no apparent RL signature are most likely ones for which the conductors are far too deep to be detected by the VTEM signal. This is consistent with the fact that the unconformity surface varies in depth from 530 m below surface on the southeast of the survey area to greater than 850 m below surface on the northwest of the survey area. Among the strongest conductors are the ones on the eastern side of the survey area. The RL signature of these conductors traces the northeast–southwest strike direction and becomes larger toward southwest before changing to a southward direction at the southern extremity of the survey area. All the main continuous RL signatures (as well as the conductors in this area) have a general northeast–southwest strike direction. Line 1660 marked in Figure 13 is chosen to show some of the inversion results on RL data using VPem3D.

Figure 14 presents a vertical slice of the 3D inverted model below this line. For our first inversion, we used a starting model made up of two homogeneous units (sandstone and basement) separated by the unconformity surface known from diamond drillholes in the region. Resistivity bounds were imposed consistent with petrophysically derived limits of resistivity for these units (Figure 3); 100–10,000 Ωm for sandstone and altered sandstone above the unconformity and 10–100,000 Ωm for basement and graphitic pelites below the unconformity. Depth weights were applied to minimize the effect of near-surface sensitivity to the inversion model. Cell sizes were 100, 300, and 100 m in the x - (along-line), y - (across-line), and z - (depth) directions, respectively. The resulting inverted model is shown in Figure 14a, whereas the observed and calculated RL data along the profile are shown in Figure 14b. The inverted model shows a broad conductivity anomaly on the southeast part of the line (between 8500 and 11,000 m) at all depths, to explain the large increase in RL (black line in the bottom plot) in this area. The highest conductivities are below the unconformity surface in this area. However, there is significant conductivity above the unconformity with lower maximum values than those below, likely due to the resistivity bounds imposed on the units during the inversion. The area to the northwest is mainly highly resistive, in line with the minor RL values in that area. In general, there is a good fit between the calculated and observed RL data with an average misfit of 0.6 pTms; however, it has to be noted that inversion models are nonunique and this represents one model among many that can potentially explain the observed data.

A more sophisticated starting model for a 3D inversion is one that is produced by interpolating 1D conductivity-depth sections. We generated conductivity-depth sections with a differential resistivity algorithm for time-domain EM, which was adapted (Greg Hodges, 2021, personal communication) from the concept of differential resistivity described for frequency-domain EM by Huang and Fraser (1996). The algorithm assumes that the apparent homogeneous half-space conductivity at each time channel can be used to define a layer of conductivity thickness equal to the skin depth and apparent conductivity of that time delay. For the first off-time channel, this layer is assumed to have constant conductivity. For each subsequent time channel, a new layer is defined by the difference in the conductivity thickness and depth defined by that channel and the conductivity thickness of the previous channel. Figure 15a shows a conductivity-depth section that was produced with this method. Using this as a starting model, Figure 15b demonstrates the conductivity-depth section below line 1660 from the 3D inversion. In this case, depth weights were not applied, but depth information was provided to the VPem3D inversion through the starting model along with the other constraints, such as the known surface of unconformity and resistivity bounds for the different units. In this model, the conductivity within the basement, in the southeast part of the line, is more compact and appears to have an apparent dip to the southeast. The

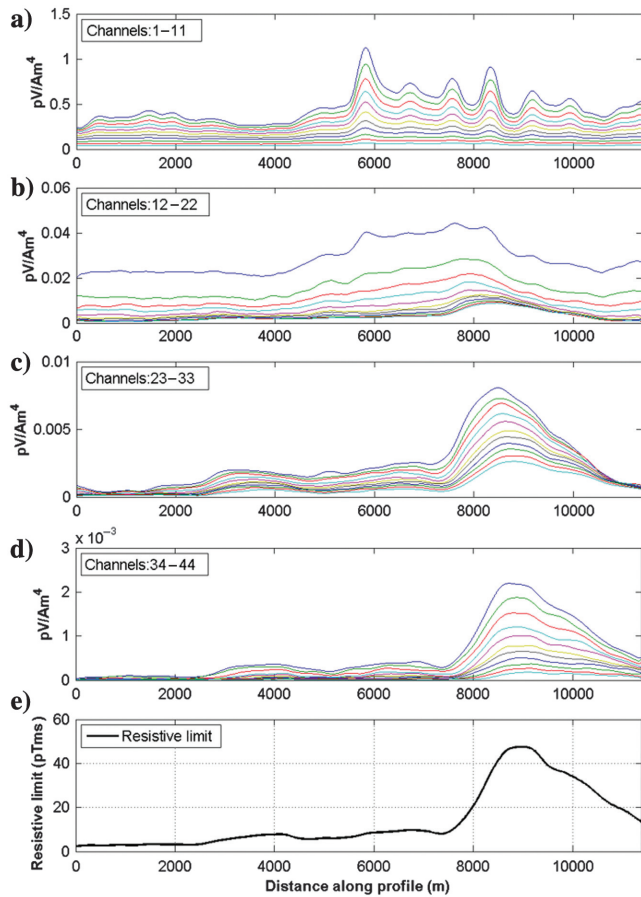


Figure 12. Sample data from line 1660 in the VTEM survey showing (a–d) all 44 channels in the magnetic field transient decay along the profile and (e) the calculated RL data for the same line along the profile. The units of RL are pTms.

basement conductor is approximately at the 9500 m position along the profile and extends from depth up to the unconformity surface. In contrast to the model of Figure 14, the sandstone area above this region is less conductive than the basement but is more conductive than the sandstone everywhere else along the line. The elevated conductivity persists right up to the surface where the overburden above the basement anomaly is also more conductive than everywhere else. A broad conductive region persists below the unconformity at depth for most of the survey line. In general, this model has more conductivity contrast than the model of Figure 14, meaning that the most conductive regions in the basement are relatively much more conductive than the most resistive regions in the sandstone. Similar to the model of Figure 14, there is a good agreement between the observed and calculated RL data and the average misfit is 1.4 pTms.

DISCUSSION

In practice, what models A, B, C, and D of Figure 4 demonstrate is that, given a shallow EM sounding system, for the case of high resistivity and specific thickness values of overburden (4000–16,000 Ωm up to 50 m thickness), it may not be possible to separately resolve the thickness and resistivity parameters of a thin resistive overburden. To resolve the conductivity-thickness product (or thickness/resistivity ratio) of the overburden, the conductivity and thickness of the underlying sandstone must be known. However, given an overburden that is more conductive than the sandstone (resistivities on the order of 1000 Ωm and thickness of 25 m), the resistivity and thickness of the overburden can be separately resolved without a priori knowledge of either of these parameters or those of the sandstone. Furthermore, it is possible to recover the

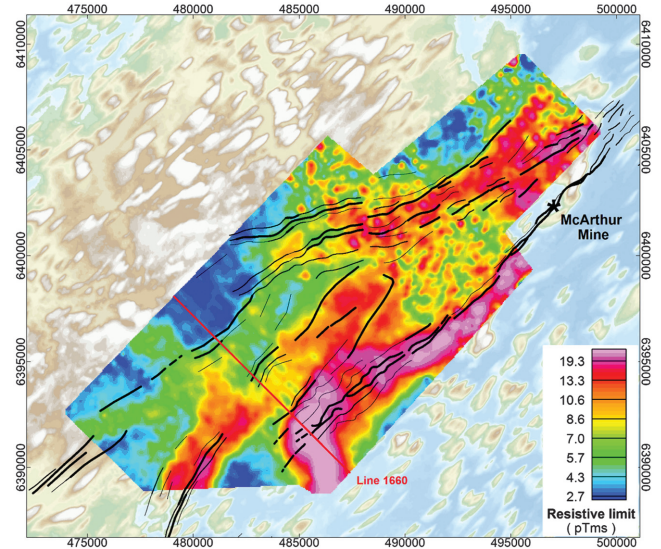


Figure 13. The RL data calculated from the time integrated magnetic field decay over the entire VTEM survey area. This is the quantity that is inverted by the VPem3D algorithm. The black lines show the location of interpreted conductors from ground EM surveys projected to the surface (from Cameco Corporation). The line width corresponds to the strength of conductor (conductivity-thickness product as interpreted from ground EM inversions), with stronger conductors represented by thicker lines. The red line indicates the position of VTEM line 1660 for which depth sections are shown in the paper.

average resistivity of the underlying sandstone with good accuracy (within approximately 15%) given high-quality data from a standard shallow EM sounding instrument. Further experiments with such synthetic models (not shown here) demonstrated that these

results hold for a wide range of typical resistivity and thicknesses in the study area, so long as there is contrast in resistivity between overburden and sandstone of at least a factor of two, and the overburden has thickness on the order of a skin depth or more at the highest transmitted frequencies in the sounding signal. Although for this study receiver noise of approximately 1 nV/m^2 was assumed, in practice, receiver noise in the field may be higher and therefore the resolving power of the data will be reduced. This will require mitigation by further stacking (increased integration time) of the data, which reduces random noise at the expense of an increase in the time taken for each sounding.

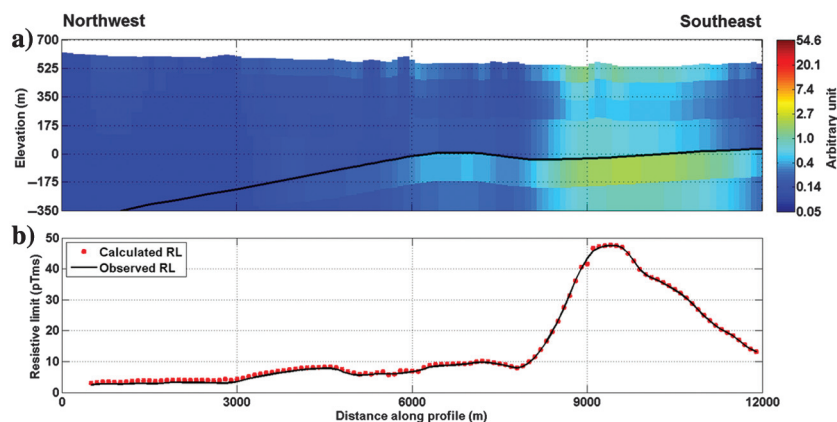


Figure 14. A conductivity section along line 1660 obtained from a 3D inversion using VPem3D with a simple starting model in which resistivity bounds were imposed for two homogeneous units (sandstone and basement) separated by the unconformity surface denoted by the black line. (a) Conductivity-depth section from VPem3D inversion. Cell sizes are 100, 300, and 100 m in the x - (along-line), y - (across-line), and z -directions, respectively. The inverted arbitrary conductivity unit is proportional to absolute conductivity unit S/m (see the “Field data” section for explanation) and (b) observed versus calculated RL data along the profile from northwest to southeast (average misfit is 0.6 pTms).

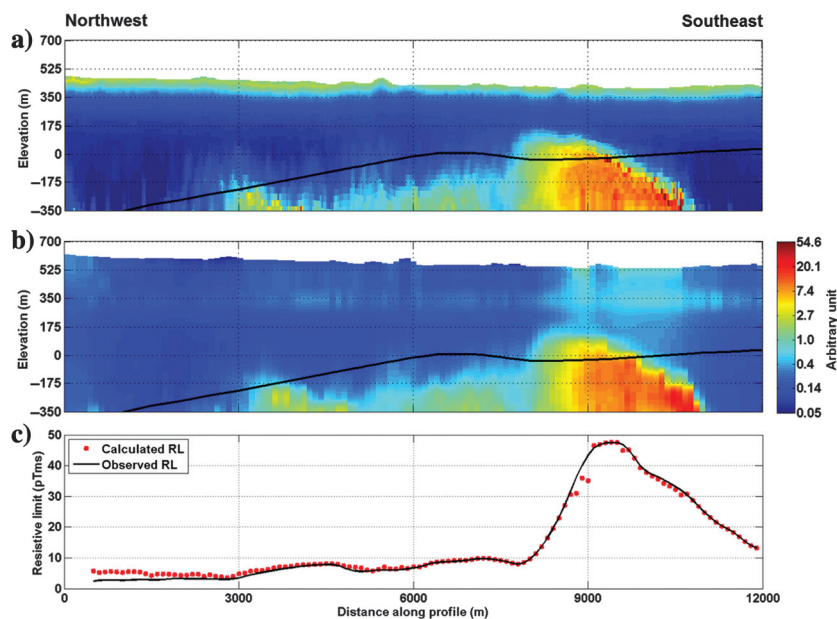


Figure 15. A conductivity section along line 1660 obtained from a 3D inversion using VPem3D with a conductivity-depth section as a starting model. The sub-Athabasca unconformity surface (black line) and resistivity bounds for sandstone and basement units were provided as constraints. (a) Starting model produced by interpolating 1D conductivity-depth sections and (b) conductivity-depth section from VPem3D inversion. Cell sizes are 100, 300, and 100 m in the x - (along-line), y - (across-line), and z -directions, respectively. The inverted arbitrary conductivity unit is proportional to absolute conductivity unit S/m (see the “Field data” section for explanation) and (c) observed versus calculated RL data along the profile from northwest to southeast (average misfit is 1.4 pTms).

Figures 7–9 together present model comparisons that examine the effect on the VTEM decay response of three features: a deep basement conductor, conductive alteration in the sandstone, and varying overburden thickness. Figure 7 confirms that a conductive target at depths greater than 600 m with the typical values of conductivity for the target and sandstone has a significant and detectable effect on the signal in the early and late channels of the VTEM system. The early channels (<15) register measurable changes of up to 10% at all positions, but as one proceeds along the profile to stations over the conductor, and the mid to late channels (>20) of the system register the largest changes — on the order of 100%–200% relative to the average of the two models E and F. When the effect of a varying overburden thickness ($\pm 20\%$) is examined in Figure 9, it is apparent that the overburden variations have no measurable effect on the late channels. This is not surprising, as the basement conductor dominates the response in these channels. However, the earliest channels (1–5) show variations of at most 10% in signal strength in response to overburden thickness changes; large enough to mask the signal from a conductor in the basement at those channels. Comparing these results with that of Figure 8, which shows that the effect of a weak conductivity anomaly in the sandstone is on the order of 10% in the early to mid-channels, would seem to suggest that such changes would be comparable with those due to overburden variations. However, the maximum measurable signal difference occurs in very different channel ranges in each case. As an example, for position 400 m in Figure 9, the maximum change due to a 20% increase in overburden thickness occurs in the early channel range of 1–5 and is approximately 5%–10%. However, in the case of alteration (position 400 m in Figure 8), although the signal difference at the same receiver location is still on the order of 5%–10%, this change occurs in the mid-channel range of 10–22. In fact, this is a pattern that is consistent at most positions: For a varying overburden model (Figure 9), the greatest changes occur at the early

channels up to 5, whereas for alteration (Figure 8), the greatest changes are found in the mid-channel range of 10–22.

Taken together, Figures 7–9 suggest that overburden thickness variations, a weak conductivity anomaly in the sandstone, and a deep conductive target in the basement, can all produce measurable VTEM responses given typical values of resistivity. However, these potential targets exert their maximum effect in different channel ranges and as such may be distinguishable from each other. In practice, whether a conductivity anomaly due to alteration in the sandstone is large enough to be detectable is dependent on the size and conductivity contrast of the volume and the survey line spacing. The small proportion of alteration minerals in the quartz-rich sandstones means that the differences in physical properties between unaltered and altered sandstones are relatively small, which emphasizes the challenge in imaging subtle alteration signatures using geophysics. These subtle signatures will be even more difficult to detect when they are above conductive features (graphitic conductors or a paleo-oregolith) or below conductive overburden.

The GPR profiles presented in Figures 10 and 11 give insights into the complexity of the Quaternary sediment cover and how its thickness varies. They provide valuable information that inform construction of EM models and interpretation of EM data. GPR-signal penetration in till in this area was higher than what is typically achieved in tills at other locations (e.g., Spagnolo et al., 2014). This is in part due to the instrument and antennas used and also because the till is particularly sandy in the study area. Nonetheless, GPR only partially penetrated through the taller drumlins and can thus only resolve the full Quaternary sediment thickness and bedrock topography in between drumlins, where stratified sediments (likely sand/gravel) occur (Figure 11). There is also organic (peat) material at the surface, but this material represents only a small area of the total Quaternary cover. The conductivity of the Quaternary cover is thus expected to vary across the study area, but it should be, on average, that of sandy till and other sandy sediments, which largely dominate the near-surface sediment successions. The GPR-L2 profile in Figure 11 also gives some insights into the water table. On this line, the most continuous reflector close to the surface is interpreted to be the water table (also confirmed by field observations). This is indicated by a blue line close to the surface at approximately 523 m above sea level at the northwest end of the profile that gently dips toward the southeast. This is an apparent slope that is likely close to the true direction of the horizontal hydraulic gradient given the regional topography shown in Figure 2. This suggests that most of the sandstone and Quaternary sediments between drumlins are saturated, whereas the sandy till higher up into the drumlins are mostly unsaturated. These variations in water content are likely to affect conductivity of the near-surface materials and could have modulated the conductivity results of the upper layer in our inversions. Interpreted GPR data, field excavations, and detailed field observations indicate that the depth of the water table varies considerably in the study area. Furthermore, there are seasonal variations in the height of the water table, with spring generally having the highest water table elevations. Based on GPR, borehole data, and drumlin heights, the thickness of Quaternary deposits in the area is estimated to range from 0 to approximately 117 m. For very thick overburden (>100 m) in the Athabasca Basin, where GPR is not able to resolve the full Quaternary sediment thickness, horizontal-to-vertical passive seismic methods have been shown to be effective in mapping the overburden (Keller, 2018).

The 3D inversion results in Figures 14 and 15 present different models for line 1660 of the VTEM survey. The nonunique nature of inversion modeling means that while the models successfully reproduce the observed RL data along the profile, they can vary considerably from each other in certain regions. The model of Figure 15, which is produced from a 1D starting model, with the constraints of unconformity and petrophysically suitable resistivity bounds for sandstone and basement, suggests that a dipping basement conductor extends from great depth up to the unconformity surface. Although at this depth (greater than 550 m below surface), and with survey line spacing of 300 m, it may not be possible to determine the dip without further constraints, the location of this conductor corresponds to the P2 conductor. The sandstone volume immediately above the basement conductor shows elevated conductivity in a broad halo that extends to the surface. This halo is anywhere from 1.5 to 2 times more conductive than the average sandstone background. Although this could potentially be an indicator of alteration, it is not the alteration system associated with the McArthur River due to its great distance from the deposit (more than 10 km). In general, the surface of unconformity roughly marks the boundary of a more conductive zone at depth in the basement and a much more resistive zone in the sandstone along most of the profile. The northwest half of the survey line is dominated by the very high resistivities of the sandstone as the unconformity proceeds to incline deeper in this region. In addition, the basement rocks below the unconformity in this area are composed mainly of quartzite, which is highly resistive. The accurate determination of overburden character as a separate unit is difficult, as Figures 14 and 15 are quite different close to the surface. A separate overburden layer was not given as a constraint to the inversion models because of a lack of good quality petrophysical data for the overburden in coverage and sample size; any estimate of the base of the overburden would have to be made from an interpolation of a very sparse set of sampled overburden thicknesses in the survey area and the adjacent regions. In addition, for thin overburden (on the order of tens of meters), the VTEM decay data may not contain much information about this region of the subsurface. This is because by the first VTEM channel at 21 μ s after the primary transmitted current turn-off ramp, the fields will already have diffused to considerable depth for moderately resistive overburden. In our models, the overburden comprises, at most, the top 10% of the vertical extent. Finally, the elevated conductivity in the sandstone up to the surface is likely a real feature, but without the support of resistivity logs from drillholes in the area, it is uncertain whether the elevated conductivity in the sandstone above the basement conductor is indicative of alteration. However, the numerous inversion models that were produced in the course of this study shared the common characteristic of elevated conductivity in the sandstone to adequately explain the VTEM data.

CONCLUSION

Through the use of 1D and 3D forward and inverse modeling and by considering different geophysical data sets, this paper attempts to determine (or constrain) features of overburden, sandstone, and basement near the McArthur River deposit in the Athabasca Basin. Several notable conclusions can be drawn from the work presented here.

When investigating the overburden cover, a shallow EM sounding system is more likely to be able to resolve separately the conductivity and thickness parameters of a conductive overburden

than those of a resistive overburden layer, given typical values for resistivity and thickness in the McArthur River area. Synthetic modeling shows that this holds for a wide range of typical resistivity and thicknesses, so long as there is at least a factor of two resistivity contrast between overburden and sandstone. However, this requires that the conductive overburden layer be inductively thick enough, meaning that its thickness must be on the order of a skin depth or more at the highest transmitted frequencies in the sounding signal, or alternatively that the diffusion depth of the EM signal must be within the layer at the earliest time channels. To independently estimate resistivity and thickness for resistive overburden, a combination of shallow EM sounding and direct current resistivity sounding or GPR could be used.

Using an AEM system, it is possible to detect a graphitic basement conductor of 20 S conductance at depths greater than 600 m below surface in the presence of moderate overburden thickness variations (conductance variations of 0.04–0.06 S) and sandstone alteration (background sandstone conductance of 0.22 S). The presence of overburden thickness variations (40–60 m) and sandstone alteration (increased sandstone conductivity by a factor of 2.5 over the average background of 0.4 mS/m) have comparable signatures in terms of VTEM signal size variations. However, the two cases are distinguishable in terms of delay time: Whereas the overburden variations cause their maximum change in the very early VTEM channels (1–5 or 21–42 μ s), the alteration signature is most evident in the mid-channel range (15–22 or 167–440 μ s). The signature of the deep conductor is most evident in the late channels (>330 μ s) of the VTEM time decay. Furthermore, converting the multichannel AEM data into RLs at each location can quickly map the lateral distribution of conductors within the AEM depth of investigation.

For the VTEM data presented in this paper, 3D inversion using the RL and an appropriate starting model has mapped a basement conductor consistent with the location and depth of the P2 fault. Furthermore, elevated conductivity of up to a factor of two over the background values, within the sandstone above this basement conductor, could possibly indicate alteration. However, actual resistivity logs in the area are needed to confirm the presence of a conductivity increase due to alteration. The cover is not well mapped in the RL inversions, but constraints from shallow EM methods or radar could improve the near-surface detail and this might help to image any alteration in the sandstone. To that end, GPR is a useful tool for assessing shallow subsurface variations of soil composition, water content, and stratigraphy (till, fine and coarse sand, clay), which cause variations of resistivity. Mapping bedrock depth and topography can be achieved by carrying out GPR surveys in the lows between drumlins. The greater Quaternary cover thicknesses are dominantly controlled by topography (taller drumlins and eskers). Therefore, a combination of high-quality DEM data, few GPR lines, and a set of sparse drillholes to constrain the top of bedrock can be used to provide a good estimate of overburden thickness. In the study area, GPR data and topography suggest that the Quaternary cover varies in thickness from 0 to approximately 117 m and consists dominantly of sandy till (moderate resistivity). The EM system modeled here should thus be applicable in this type of terrain, which is likely similar to many other prospective areas across the basin. In areas where the overburden is very resistive, GPR (or other methods such as high-resolution S-wave seismic surveys), could be used to map the overburden thickness. The use of GPR and other shallow EM sounding tools to map resistivity and

thickness of overburden can provide constraints for interpretation of deeper EM data.

ACKNOWLEDGMENTS

The authors would like to thank Cameco Corporation for providing us with proprietary geophysical data and expert advice, in particular, G. Wood and C. O'Dowd, who offered helpful guidance and suggestions during the project, and G. Zaluski and C. Keller, who provided us with valuable feedback on the manuscript. We are also grateful for the support of CGG and G. Hodges, who provided software for the 1D inversion of VTEM data. We further thank Geosoft Inc. (now part of Seequent) for providing support by making the Oasis Montaj software freely available for use during the course of this project. In addition, we thank W. Pun and H. Ugalde of Paterson, Grant & Watson Limited, who assisted in data processing and interpretation. In addition, we thank our colleagues involved in the CMIC Footprints project for fruitful discussions and comments on this work during meetings and conferences. Funding was provided by the Natural Sciences and Engineering Research Council of Canada and the Canada Mining Innovation Council through a grant from the NSERC Collaborative Research and Development Program, NSERC-CMIC Mineral Exploration Footprints Project Contribution 198.

DATA AND MATERIALS AVAILABILITY

Data associated with this research are confidential and cannot be released.

REFERENCES

- Adlakha, E. E., K. Hattori, G. Zaluski, and T. M. Kotzer, 2015, Mineralogy of a fertile fluid conduit related to unconformity-type uranium deposits in the Athabasca Basin, Saskatchewan: Targeted Geoscience Initiative, **4**, 74–82, doi: [10.4095/295776](https://doi.org/10.4095/295776).
- Alexandre, P., K. Kyser, P. Polito, and D. Thomas, 2005, Alteration mineralogy and stable isotope geochemistry of Paleoproterozoic basement — Hosted unconformity-type uranium deposits in the Athabasca Basin, Canada: Economic Geology, **100**, 1547–1563, doi: [10.2113/gsecongeo.100.8.1547](https://doi.org/10.2113/gsecongeo.100.8.1547).
- Alexandre, P., K. Kyser, D. Thomas, P. Polito, and J. Marlatt, 2009, Geochronology of unconformity-related uranium deposits in the Athabasca Basin, Saskatchewan, Canada and their integration in the evolution of the basin: Mineralium Deposita, **44**, 41–59, doi: [10.1007/s00126-007-0153-3](https://doi.org/10.1007/s00126-007-0153-3).
- Annesley, I. R., C. Madore, and P. Portella, 2005, Geology and tectonic evolution of the western margin of the Trans-Hudson Orogen: Evidence from the eastern sub-Athabasca basement, Saskatchewan: Canadian Journal of Earth Sciences, **42**, 573–597, doi: [10.1139/e05-034](https://doi.org/10.1139/e05-034).
- Ansari, S. M., and C. G. Farquharson, 2013, 3D finite-element forward modeling of electromagnetic data using vector and scalar potentials and unstructured grids: Geophysics, **79**, no. 4, E149–E165, doi: [10.1190/geo2013-0172.1](https://doi.org/10.1190/geo2013-0172.1).
- Ansdell, K. M., 2005, Tectonic evolution of the Manitoba-Saskatchewan segment of the Paleoproterozoic Trans-Hudson Orogen, Canada: Canadian Journal of Earth Sciences, **42**, 741–759, doi: [10.1139/e05-035](https://doi.org/10.1139/e05-035).
- Bronkhorst, D., A. G. Mainville, G. M. Murdock, and L. D. Yesnik, 2012, McArthur River Operation, Northern Saskatchewan, Canada: National Instrument 43-101, Technical Report, Prepared for Cameco Corporation.
- Campbell, J. E., 2007, Quaternary geology of the eastern Athabasca Basin, Saskatchewan, in C. W. Jefferson and G. Delaney, eds., EXTECH IV: Geology and uranium exploration technology of the proterozoic Athabasca Basin, Saskatchewan and Alberta: Bulletin 588 of the Geological Survey of Canada, 211–228.
- Card, C., and P. Heath, 2015, Bedrock geology of sub-Athabasca basement rocks (NTS 74H): Saskatchewan Geological Survey, Saskatchewan Ministry of the Economy, Geoscience Map 2015-1.
- Cassidy, N., 2009, Ground penetrating radar data processing, modelling and analysis, in H. Jol, ed., Ground penetrating radar: Elsevier, 141–176.

- Cloutier, J., K. Kyser, G. R. Olivo, P. Alexandre, and J. Halaburda, 2009, The Millennium uranium deposit, Athabasca Basin, Saskatchewan, Canada: An atypical basement-hosted unconformity-related uranium deposit: *Economic Geology*, **104**, 815–840, doi: [10.2113/gsecongeo.104.6.815](https://doi.org/10.2113/gsecongeo.104.6.815).
- Corrigan, D., S. Pehrsson, N. Wodicka, and E. de Kemp, 2009, The Palaeoproterozoic Trans-Hudson Orogen: A prototype of modern accretionary processes: *Geological Society Special Publication* 327, 457–479.
- Darjani, M., 2019, Investigating modelling and inversion techniques for overburden stripping for uranium exploration in the Athabasca Basin, Canada: Department of Earth Sciences, Memorial University of Newfoundland, 298.
- Farquharson, C. G., and D. W. Oldenburg, 1993, Inversion of time-domain electromagnetic data for a horizontally layered earth: *Geophysical Journal International*, **114**, 433–442, doi: [10.1111/j.1365-246X.1993.tb06977.x](https://doi.org/10.1111/j.1365-246X.1993.tb06977.x).
- Farquharson, C. G., and D. W. Oldenburg, 1996, Approximate sensitivities for the electromagnetic inverse problem: *Geophysical Journal International*, **126**, 235–252, doi: [10.1111/j.1365-246X.1996.tb05282.x](https://doi.org/10.1111/j.1365-246X.1996.tb05282.x).
- Farquharson, C. G., and D. W. Oldenburg, 2004, A comparison of automatic techniques for estimating the regularization parameter in non-linear inverse problems: *Geophysical Journal International*, **156**, 411–425, doi: [10.1111/j.1365-246X.2004.02190.x](https://doi.org/10.1111/j.1365-246X.2004.02190.x).
- Farquharson, C. G., and D. W. Oldenburg, 2006, EM1DTM: A program library for forward modelling and inversion of time domain electromagnetic data over 1D structures: UBC-Geophysical Inversion Facility, Department of Earth and Ocean Sciences, University of British Columbia.
- Farquharson, C. G., D. W. Oldenburg, and P. S. Routh, 2003, Simultaneous 1D inversion of loop-loop electromagnetic data for magnetic susceptibility and electrical conductivity: *Geophysics*, **68**, 1857–1869, doi: [10.1190/1.1635038](https://doi.org/10.1190/1.1635038).
- Fullagar, P. K., and G. A. Pears, 2007, Towards geologically realistic inversion, in B. Milkereit, ed., *Proceedings of Exploration '07*, Fifth Decennial International Conference on Mineral Exploration, 444–460.
- Fullagar, P. K., and R. Schaa, 2014, Fast 3D inversion of transient electromagnetic (TEM) resistive limit data: 84th Annual International Meeting, SEG, Expanded Abstracts, 4366–4370, doi: [10.1190/segam2014-1157.1](https://doi.org/10.1190/segam2014-1157.1).
- Hiatt, E. E., and K. Kyser, 2007, Sequence stratigraphy, hydrostratigraphy, and mineralizing fluid flow in the Proterozoic Manitou Falls Formation, eastern Athabasca Basin, Saskatchewan, in C. W. Jefferson and G. Delaney, eds., *EXTECH IV: Geology and uranium exploration technology of the proterozoic Athabasca Basin*, Saskatchewan and Alberta: Bulletin 588 of the Geological Survey of Canada, 489–506.
- Hillier, J. K., M. J. Smith, C. D. Clark, C. R. Stokes, and M. Spagnolo, 2013, Subglacial bedforms reveal an exponential size-frequency distribution: *Geomorphology*, **190**, 82–91, doi: [10.1016/j.geomorph.2013.02.017](https://doi.org/10.1016/j.geomorph.2013.02.017).
- Hoeve, J., and T. I. I. Sibbald, 1978, On the genesis of rabbit lake and other unconformity-type uranium deposits in Northern Saskatchewan, Canada: *Economic Geology*, **73**, 1450–1473, doi: [10.2113/gsecongeo.73.8.1450](https://doi.org/10.2113/gsecongeo.73.8.1450).
- Huang, H., and D. C. Fraser, 1996, The differential parameter method for multifrequency airborne resistivity mapping: *Geophysics*, **61**, 100–109, doi: [10.1190/1.1574674](https://doi.org/10.1190/1.1574674).
- IAEA, 2018, Unconformity-related uranium deposits: International Atomic Energy Agency.
- Jeanneret, P., P. Goncalves, C. Durand, P. Trap, D. Marquer, D. Quirt, and P. Ledru, 2016, Tectono-metamorphic evolution of the pre-Athabasca basement within the Wollaston–Mudjatik transition zone, Saskatchewan: *Canadian Journal of Earth Sciences*, **53**, 231–259, doi: [10.1139/cjes-2015-0136](https://doi.org/10.1139/cjes-2015-0136).
- Jefferson, C. W., D. Thomas, S. S. Gandhi, P. Ramaekers, G. Delaney, D. Brisbin, C. Cutts, P. Portella, and R. A. Olson, 2007, Unconformity-associated uranium deposits of the Athabasca basin, Saskatchewan and Alberta, in C. W. Jefferson and G. Delaney, eds., *EXTECH IV: Geology and uranium exploration technology of the proterozoic Athabasca Basin*, Saskatchewan and Alberta: Bulletin 588 of the Geological Survey of Canada, 23–67.
- Jones, D., S. M. Ansari, C. G. Farquharson, and R. B. Hearst, 2016, Synthesizing time-domain electromagnetic data for graphitic fault zones and associated uranium deposits in the Athabasca Basin, Canada: 86th Annual International Meeting, SEG, Expanded Abstracts, 2206–2210, doi: [10.1190/segam2016-13866371.1](https://doi.org/10.1190/segam2016-13866371.1).
- Keller, C., 2018, The H/V passive seismic method for mapping glacial overburden thickness: Saskatchewan Geological Survey Open House 2018 Abstract Volume, Miscellaneous Report 2018-3, Saskatchewan Ministry of Energy and Resources.
- Long, S. R. M., R. S. Smith, and R. B. Hearst, 2017, Ground resistivity method and DCIP2D forward and inversion modelling to identify alteration at the Midwest uranium deposit, northern Saskatchewan, Canada: *Exploration Geophysics*, **48**, 383–393, doi: [10.1071/EG15059](https://doi.org/10.1071/EG15059).
- MacDonald, C., T. I. I. Sibbald, and W. Petruk, 1985, Mineralogy and geochemistry of the sub-Athabasca regolith near Wollaston Lake: *Canadian Institute of Mining and Metallurgy*, **32**, 155–158.
- Macnae, J. C., A. King, N. Stolz, and P. Klinkert, 1999, 3-D EM inversion to the limit, in M. Oristaglio and B. Spies, eds., *Three-dimensional electromagnetics*: SEG, 489–501, doi: [10.1190/1.9781560802154.fm](https://doi.org/10.1190/1.9781560802154.fm).
- Matthews, R. B., R. Koch, M. Leppin, B. Powell, V. J. Sopuck, and A. G. Gubins, 1997, Advances in integrated exploration for unconformity uranium deposits in Western Canada: *Proceedings of the Exploration*, 993–1024.
- McGill, B. D., J. Marlatt, R. B. Matthews, V. J. Sopuck, L. A. Homeniuk, and J. J. Hubregtse, 1993, The P2 North uranium deposit, Saskatchewan, Canada: *Exploration & Mining Geology*, **2**, 321–331.
- McMullan, S. R., R. B. Matthews, and P. Robertshaw, 1987, Exploration geophysics for Athabasca uranium deposits: *Proceedings of the Exploration*, 547–566.
- Nabighian, M. N., and J. C. Macnae, 1991, Time domain electromagnetic prospecting methods, in M. N. Nabighian, ed., *Electromagnetic methods in applied geophysics*: SEG, 427–520.
- Newman, G. A., G. W. Hohmann, and W. L. Anderson, 1986, Transient electromagnetic response of a three-dimensional body in a layered earth: *Geophysics*, **51**, 1608–1627, doi: [10.1190/1.1442212](https://doi.org/10.1190/1.1442212).
- Ng, R., P. Alexandre, and K. Kyser, 2013, Mineralogical and geochemical evolution of the unconformity-related McArthur river zone 4 orebody in the Athabasca Basin, Canada: Implications of a silicified zone: *Economic Geology*, **108**, 1657–1689, doi: [10.2113/econgeo.108.7.1657](https://doi.org/10.2113/econgeo.108.7.1657).
- Powell, B., G. Wood, L. Bzdel, and B. Milkereit, 2007, Advances in geophysical exploration for uranium deposits in the Athabasca Basin: *Proceedings of the Exploration*, 771–790.
- Ramaekers, P., and O. Catuneanu, 2004, Development and sequences of the Athabasca Basin, Early Proterozoic, Saskatchewan and Alberta, Canada, in P. G. Eriksson, W. Altermann, D. R. Nelson, W. U. Mueller, and O. Catuneanu, eds., *The Precambrian earth: Tempos and events*: Elsevier Science Ltd., 705–723.
- Ramaekers, P., C. W. Jefferson, G. M. Yeo, B. Collier, D. G. F. Long, G. Drever, S. McHardy, D. Jiricka, C. Cutts, K. Wheatley, O. Catuneanu, S. Bernier, B. Kupsch, and R. T. Post, 2007, Revised geological map and stratigraphy of the Athabasca group, Saskatchewan and Alberta, in C. W. Jefferson and G. Delaney, eds., *EXTECH IV: Geology and uranium exploration technology of the proterozoic Athabasca Basin*, Saskatchewan and Alberta: Bulletin 588 of the Geological Survey of Canada, 155–191.
- Reid, J. E., and J. C. Macnae, 2002, Resistive limit modeling of airborne electromagnetic data: *Geophysics*, **67**, 492–500, doi: [10.1190/1.1468609](https://doi.org/10.1190/1.1468609).
- Rogers, S., N. Bridge, C. O'Dowd, H. Yang, A. Aubin, and A. Yackulic, 2017, Geological framework of the Fox Lake uranium deposits, eastern Athabasca Basin, Canada, Saskatchewan Geological Survey Open House 2017 Abstract Volume, Miscellaneous Report 2017-3, Saskatchewan Ministry of Energy and Resources.
- Scott, S., M. Ross, M. Chouteau, P. Shamsipour, H. Chen, J. E. Campbell, T. M. Kotzer, D. Quirt, and K. Kyser, 2017, Till stratigraphy in the drumlinized terrain of the McArthur River uranium mine area in the eastern Athabasca Basin: GAC-MAC Abstracts, 340–341.
- Smith, R. S., G. Wood, and B. Powell, 2010, Detection of alteration at the Millennium uranium deposit in the Athabasca Basin: A comparison of data from two airborne electromagnetic systems with ground resistivity data: *Geophysical Prospecting*, **58**, 1147–1158, doi: [10.1111/j.1365-2478.2010.00880.x](https://doi.org/10.1111/j.1365-2478.2010.00880.x).
- Spagnolo, M., E. C. King, D. W. Ashmore, B. R. Rea, J. C. Ely, and C. D. Clark, 2014, Looking through drumlins: Testing the application of ground-penetrating radar: *Journal of Glaciology*, **60**, 1126–1134, doi: [10.3189/2014JG14J110](https://doi.org/10.3189/2014JG14J110).
- Stolz, E. M., and J. C. Macnae, 1997, Fast approximate inversion of TEM data: *Exploration Geophysics*, **28**, 317–322, doi: [10.1071/EG997317](https://doi.org/10.1071/EG997317).
- Tran, H. T., K. M. Ansdell, K. M. Bethune, K. Ashton, and M. A. Hamilton, 2008, Provenance and tectonic setting of Paleoproterozoic metasedimentary rocks along the eastern margin of Heame craton: Constraints from SHRIMP geochronology, Wollaston Group, Saskatchewan, Canada: *Precambrian Research*, **167**, 171–185, doi: [10.1016/j.precamres.2008.08.003](https://doi.org/10.1016/j.precamres.2008.08.003).
- Vallée, M. A., W. A. Morris, S. Perrouty, R. G. Lee, K. Wasyliuk, J. J. King, K. M. Ansdell, R. Mir, P. Shamsipour, C. G. Farquharson, M. Chouteau, R. J. Enkin, and R. S. Smith, 2019, Geophysical inversion contributions to mineral exploration: Lessons from the footprints project: *Canadian Journal of Earth Sciences*, **56**, 525–543, doi: [10.1139/cjes-2019-0009](https://doi.org/10.1139/cjes-2019-0009).

Biographies and photographs of the authors are not available.